



On the hydrodynamic response and slamming impact of a cylindrical FPSO in combined wave-current flows

Shuaiwen Huo^a, Shi Deng^b, Zhengrong Song^b, Weiwen Zhao^{a,*}, Decheng Wan^a

^a Computational Marine Hydrodynamic Lab (CMHL), School of Naval Architecture, Ocean and Civil Engineering, Shanghai Jiao Tong University, Shanghai, 200240, China

^b Offshore Oil Engineering Co. Ltd., Tianjin, 300450, China

ARTICLE INFO

Handling Editor: Prof. A.I. Incecik

Keywords:

Cylindrical FPSO
Wave generating-absorbing boundary condition
Combined wave-current
Vortex shedding
Impact pressure

ABSTRACT

Owing to the lower construction and transportation costs, cylindrical floating production storage offloading (CFPSO) has received extensive attention in the industry. Currently, attention has primarily been focused on the damping performance of heave plate while few studies have touched upon hydrodynamic characteristics under complex combined wave-current condition. In this paper, we numerically investigate the hydrodynamic response and slamming impact of a CFPSO under combined wave-current flows. The active wave generating-absorbing boundary condition (GABC) along with the buoyancy-modified k- ω SST turbulence model are utilized to generate high-precision waves and current based on the open source computational fluid dynamics (CFD) framework OpenFOAM. A self-developed six degree of freedom (6DOF) motion module is used for solving rigid body motion and updating mesh motion. The numerical results of motion response and impact pressure are compared with the experimental data to verify the accuracy of present simulations. The correlation between impact pressure and relative wave elevation and wave velocity is analyzed and three types of slamming events have been identified. The flow fields such as vorticity, pressure and streamlines in the vicinity of the CFPSO are also presented and discussed, which provides a reference for structural design for the CFPSO under complex sea conditions.

1. Introduction

Cylindrical floating production storage offloading (CFPSO) is a new type of offshore oil and gas exploitation equipment first built in 2006 (Seok et al., 2020). Compared with the traditional ship-type FPSOs, CFPSOs have a simpler structure, resulting in lower production and construction costs (Hong et al., 2011). In addition, the highly symmetrical structure of CFPSOs greatly improves the utilization of its internal space and can avoid complex turret and swivel technology (Amin et al., 2022). Although CFPSOs have great industrial application value in the future, their heave natural period is always close to the wave nature period, resulting in poor heave motion performance (Afriana, 2011). Therefore, in the industrial field, a heave plate is usually added to the bottom end of the CFPSOs to improve its heave damping performance. Studies showed that heave plates can reduce the peak heave RAO by up to 50% (Amin et al., 2022). Most of the current researches on CFPSOs are always focused on the damping performance for the heave plates by computational fluid dynamics (CFD) method or experimental fluid

dynamics (EFD). Avalos and Wanderley (2018) conducted a study on the influence of bilge keel width and form on the roll damping of CFPSO sections using the CFD method. Ji et al. (2019) used CFD method to investigate the effect of the cone angle and aperture of the heave plate on the heave suppression. The research results showed that the pitch damping decreases with increasing cone angle and decreasing aperture. Jiang et al. (2020) used the CFD method to explore the influence of the width of heave plate on the CFPSO heave damping and provided suggestions for the optimization of the heave plate structure. The experimental study of the free decay of a novel deep-draft multi-column FDPSO was studied by Gu et al. (2017). The nature period and the dimensionless damping coefficient of the platform were measured out by the free decay experiment.

CFPSOs are moored in the deep sea, facing complex combined wave-current sea conditions. Many scholars used EFD method or potential flow theory to study the motion response and wave force of a CFPSO under the action of waves or ocean currents. Deng et al. (2022a) conducted a model test and compared the motion of a CFPSO under the

* Corresponding author.

E-mail address: weiwen.zhao@sjtu.edu.cn (W. Zhao).

conditions of regular wave and combined wave-current with the same encounter frequency, and found out that the heave and roll motions under combined wave-current condition were slightly larger than the amplitudes under wave only condition. Using physical model experiments, [Gonc alves et al. \(2009\)](#) constructed a database of the vortex-induced motions (VIM) results of the MonoGoM platform (a cylindrical floating device designed for the Gulf of Mexico) for comparison with theoretical and numerical models of VIM predictions. This database can help determine the undetermined parameters required to be determined in theoretical simulations and potential flow simulations.

The potential flow simulation method is known for its computational efficiency, but it has limitations in accurately reflecting the effects of viscosity. This is because the Morrison formula used in the potential flow method does not take into account the viscous effect. To obtain more accurate results, a reasonable viscous correction is required, which often involves determining a viscosity correction coefficient through model tests or the experience of engineers. Therefore, the results obtained by potential flow theory often have certain errors. [Afriana \(2011\)](#) used the potential flow simulation software *Hydro D* to analyze the motion results of CFPSO under the coupled sea state of wind, wave and current both in time domain and frequency domain. [Deng et al. \(2022b\)](#) used numerical and experimental methods to study the hydrodynamic characteristics of a CFPSO under wave, current and combined wave and current conditions. However, the simulation results under the coupled condition had certain errors compared with the experimental results, which the authors attributed to inaccuracies in the lift coefficient values.

In order to realize the accurate numerical simulation of the combined wave-current condition of the CFPSO, the first step is to establish an accurate and efficient numerical wave tank. The relaxation zone method is suitable for wave generation and absorption. However, it also increases the computational domain and time cost in the simulation process ([Higuera et al., 2013](#)). It is noteworthy that the use of relaxation zones in complex, irregular combined wave and current condition is a serious disadvantage. As the range of the relaxation region increases, the computation time required to evaluate the linear superposition of wave harmonics also increases. This includes repeatedly computing trigonometric and hyperbolic functions, which are computationally expensive ([Dimakopoulos et al., 2016](#)). In addition, determining the range of relaxation zone is a tricky problem due to the uncertainty of irregular waves. For long-term CFD numerical simulation, the size of the relaxation zone is a crucial parameter that needs to be carefully selected. If the range of the relaxation zone is too large, it will lead to a waste of computing resources. If the range of the relaxation zone is too small, the wave energy can't be fully dissipated before reaching the exit, resulting in wave reflection and surface elevation. To address this issue, this paper adopts a new active wave generating-absorbing boundary condition (GABC) proposed by [Borsboom and Jacobsen \(2021\)](#). [Chen et al. \(2022\)](#) have used the GABC wave generation and absorption method to study the phenomenon of high-frequency scattered waves of finite-length cylinders under the action of focused waves, and obtained credible simulation results.

For the CFD simulation of the combined action of waves and currents, the turbulence model can provide support for the analysis of the vortex structure around the CFPSO. However, the use of a conventional turbulence model can lead to abnormal dissipation of turbulent energy at the free surface during wave propagation, resulting in a decrease in wave elevation, which is particularly critical for high-frequency waves. To address this issue, this paper uses a buoyancy-modified *k-omega SST* turbulence model based on the *k-omega SST* turbulence model ([Van Maele and Merci, 2006](#)). This turbulence model can reduce the turbulent viscosity near the wave surface to reduce the dissipation of turbulence. [Devolder et al. \(2017\)](#) compared the numerical results using the buoyancy-modified *k-omega SST* turbulence model with the model test results of wave climbing around a single pile under regular waves and found that the buoyancy modified *k-omega SST* turbulence model provides accurate results.

In this paper, a study is conducted using CFD to investigate the hydrodynamic characteristics of the CFPSO under combined wave-current condition. On the basis of the open-source framework OpenFOAM, the new approach suitable for large-scale ocean platforms is developed by combining the GABC method, self-developed 6DOF motion module and buoyancy-modified *k-omega SST* turbulence model. The numerical results of 6DOF motion and wave impact pressure are compared with the experimental results to confirm the feasibility of this approach. In addition, the correlation between impact pressure and 6DOF motion and the vorticity field near the heave suppression structure are also analyzed. The study in this paper provides a CFD approach for the hydrodynamic characteristics of the CFPSO under complex coupled sea conditions, and offers a basic reference for the structural design of the CFPSO.

2. Numerical methods

In this paper, we use an incompressible two-phase flow CFD solver naoe-FOAM-SJTU ([Zhao et al., 2020](#); [Wang and Wan, 2018](#); [Wang et al., 2019](#)), based on OpenFOAM, to perform the numerical study of the CFPSO motion response in combined wave-current condition. The interfaces of the two-phase flow are captured using a VOF method ([Rusche, 2002](#)). The GABC method is employed to generate and absorb waves. A self-developed 6DOF motion and mooring system module combined with the moving mesh technology is utilized to realize the motion of the floating body. The buoyancy-modified *k-omega SST* turbulence model is used to reduce dissipation of the turbulent flow near the interface. Since many of the numerical methods covered in this paper is the basic methodology of CFD which can be found in many literatures and books. This paper mainly introduces the GABC method and the buoyancy-modified *k-omega SST* turbulence model, which are the most important numerical methods in this paper.

2.1. GABC method

The GABC method is a new active wave generation and absorption method implemented by [Borsboom and Jacobsen \(2021\)](#) in the wave2Foam third-party open-source code library for OpenFOAM. This method can save a lot of time compared to the relaxation zone method when dealing with complex combined wave-current conditions, which has great advantages for practical simulations of complex engineering flow.

GABC adopts the boundary input wave generation method, in which the time-varying water quality point velocity is set at the inlet boundary grid node. The irregular wave used in this paper is formed by the superposition of a large number of first-order Stokes linear waves. By using the potential flow theory, the wave surface equation of irregular waves can be deduced, considering only waves propagating in one direction, and taking the water surface as a reference.

$$\eta = \sum_{i=1}^n \frac{H_i}{2} \cos(k_i x - \omega_i t + \varphi_i). \quad (1)$$

In this study, the direction of the current is the same as the direction of wave propagation, so the velocity in the horizontal direction is the superposition of the wave velocity and the constant current velocity:

$$U = \sum_{i=1}^n \frac{\pi H_i}{T_i} \frac{\cosh k_i(z+d)}{\sinh k_i d} \cos(k_i x - \omega_i t + \varphi_i) + u_{current}, \quad (2)$$

The velocity in the vertical direction is:

$$W = \sum_{i=1}^n \frac{\pi H_i}{T_i} \frac{\sinh k_i(z+d)}{\sinh k_i d} \sin(k_i x - \omega_i t + \varphi_i), \quad (3)$$

where, H_i is the wave height of the component wave of the i -th frequency, T is the wave period of the component wave of the i -th

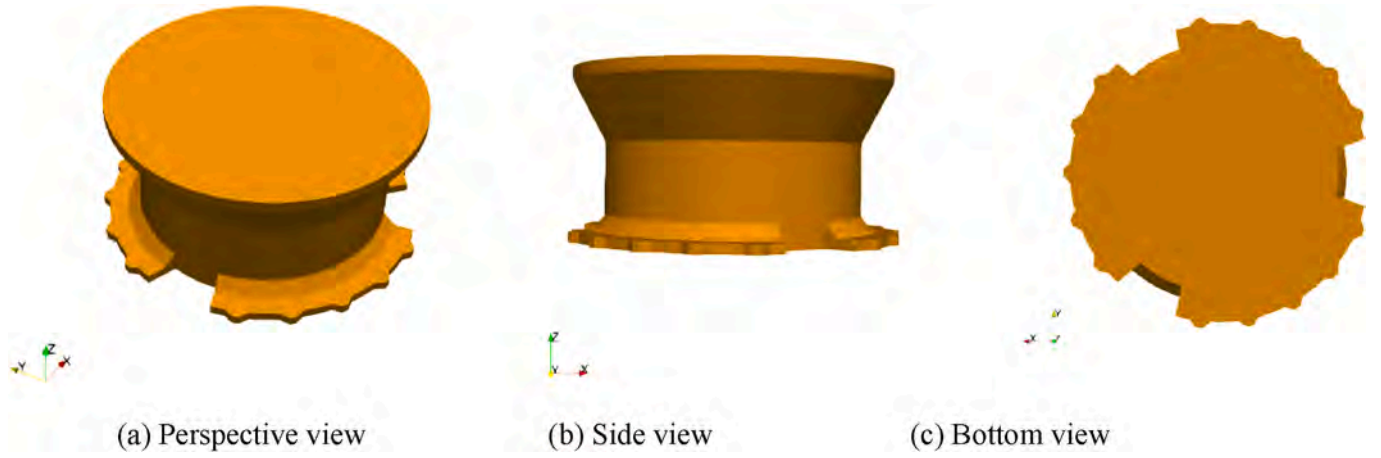


Fig. 1. Geometric model of the CFPSO.

frequency, k_i is the wave number of the component wave of the i -th frequency, ω_i is the wave circular frequency of the component wave of the i -th frequency, d is the water depth, $u_{current}$ is the current velocity.

GABC method is a modified Sommerfeld boundary condition based on the potential flow theory (Sommerfeld, 1949). The Sommerfeld boundary condition assumes that the boundary is far enough away from the structure such that the local flow is irrotational. When the flow field at the outlet satisfies the following conditions, the boundary is free of reflections.

$$\frac{\partial \varphi}{\partial t} + c \frac{\partial \varphi}{\partial x} = 0, \quad (4)$$

where φ is the velocity potential at the exit of the flow field, c is the phase velocity.

The Sommerfeld boundary condition applies only to waves with constant phase velocity. For dispersive waves, Borsboom and Jacobsen (2021) proposed to use a depth-dependent function instead of a constant value c .

$$\frac{\partial \varphi}{\partial t} + \sqrt{gd}a(z) \frac{\partial \varphi}{\partial x} = 0, \quad (5)$$

where g is the acceleration of gravity, $a(z)$ is a function related to the water depth z .

After continuous exploration by scholars, the function expression of $a(z)$ is as follows:

$$a(z) = \sum_{m=0}^3 \alpha_m \left(\frac{z}{d} + 1 \right)^m, \quad (6)$$

where α_m is a parameter to be determined, which should make sure the reflection coefficient as small as possible.

GABC uses the linear Bernoulli equation to introduce the velocity potential into the N-S equation:

$$p = -\rho_{water}gz - \rho_{water} \frac{\partial \varphi}{\partial x}, \quad (7)$$

More details of the GABC method can refer to the papers by Borsboom and Jacobsen (2021) and Chen et al. (2022).

2.2. Turbulence model

At the interface of two-phase flow, a sudden change in density can result in a significant velocity gradient. This can cause an abnormal increase in turbulent kinetic energy and turbulent viscosity, leading to excessive wave damping. To address this shortcoming of the standard k - ω SST turbulence model (Menter, 1992), a buoyancy term based on

the standard gradient diffusion hypothesis (SGDH) is added to the turbulent kinetic energy (TKE) equation to account for the sudden change in density at the interface (Van Maele and Merci, 2006).

Based on the above considerations, after the buoyancy modification of the TKE equation of the standard k - ω SST, we get the following equation:

$$\frac{\partial \rho k}{\partial t} + \frac{\partial \rho u_j k}{\partial x_j} - \frac{\partial}{\partial x_j} \left[\rho (\nu + \sigma_k \nu_t) \frac{\partial k}{\partial x_j} \right] = \rho P_k + G_b - \rho \beta^* \omega k, \quad (8)$$

$$G_b = -\frac{\nu_t}{\sigma_t} \frac{\partial \rho}{\partial x_j} g_j, \quad (9)$$

$$\frac{\partial \omega}{\partial t} + \frac{\partial u_j \omega}{\partial x_j} - \frac{\partial}{\partial x_j} \left[(\nu + \sigma_\omega \nu_t) \frac{\partial \omega}{\partial x_j} \right] = \frac{\gamma}{\nu_t} G - \beta \omega^2 + 2(1 - F_1) \frac{\sigma_{\omega 2}}{\omega} \frac{\partial k}{\partial x_j} \frac{\partial \omega}{\partial x_j}, \quad (10)$$

$$G = \nu_t \frac{\partial u_i}{\partial x_j} \left(\frac{\partial u_i}{\partial x_j} + \frac{\partial u_j}{\partial x_i} \right), \quad (11)$$

where equation (8) is the transport equation of the TKE, k ; equation (10) is the transport equation of the turbulent dissipation rate, ω . P_k is the production term of k , ν is the kinematic viscosity, ν_t is the turbulent kinematic viscosity, F_1 is the first blending functions, β^* , β , σ_k , σ_ω , $\sigma_{\omega 2}$, γ are model constants, σ_t is a scalar constant which determines the degree of buoyancy correction, and its value is 0.85 in dealing with the two-phase flow of water and air.

After solving the transport equation above, the turbulent viscosity is given by:

$$\nu_t = \frac{a_1 k}{\max(a_1 \omega, SF_2)}, \quad (12)$$

where, S is the mean strain rate of flow velocity, F_2 is the second blending functions, a_1 is a model constant.

The analysis of the above formula shows that at the free surface, the solved ν_t will approach zero due to the large increase of the vertical density gradient. In the pure liquid phase or pure gas phase computational domain, G_b tends to be zero due to the small density gradient. At this time, the buoyancy-modified k - ω SST turbulence model will degenerate into standard k - ω SST turbulence model.

3. Numerical step

3.1. Geometry

The numerical simulation in this paper used the same geometric model as the one used in the model test conducted by Offshore Oil

Table 1
Main parameters of the CFPSO model.

Parameter name	Unit	Model scale
Full load draft	m	0.380
Drainage weight	t	0.457
Pitch inertia radius	m	0.354
Diameter of platform at waterline surface	m	1.2
Heave nature frequency	Hz	0.516
Pitch nature frequency	Hz	0.262

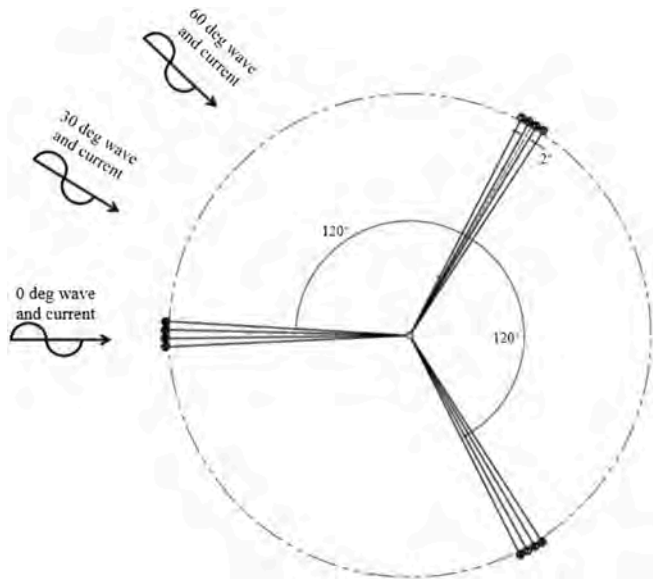


Fig. 2. Mooring system of the CFPSO.

Engineering Co., Ltd (Deng et al., 2022b) to enable a direct comparison with the test results. The 6DOF motions of CFPSO are completely free during simulations. Fig. 1 shows the perspective, side and bottom views of the numerical model. The damping plate of this CFPSO has a conical structure, and the operating water depth of the model scale is 5.25m. Table 1 provides the main parameters of the CFPSO model.

3.2. Mooring configuration

As shown in Fig. 2, the CFPSO studied in this paper is moored in the required working position by 12 moorings. The 12 moorings are divided into 3 sets, with an angle of 120° between each set. Each set contains 4 moorings with an angle of 2° between each mooring line. The mooring lines are in pretension state, with a pretention force of 2049.68 kN. To ensure the accuracy of the numerical simulation, the parameters of the numerical model of the anchor chain should be as consistent as possible with the physical model used in the test. The simulation of mooring

Table 2
Segments of a mooring line.

No.	Segment	Length (m)	Diameter (m)	Mass in water (kg/m)	Stiffness (kN)
1	Bottom Chain	200.0	0.160	449.5	2.070E6
2	Link	1.1	–	2950.0	1.958E6
3	Polyester	700.0	0.274	13.5	2.706E5
4	Link	15.6	0.283	684.1	–
5	Buoy	–	–	Net buoy 46 t	–
6	Polyester	1371.0	0.274	13.5	2.706E5
7	Link	1.1	–	3500.0	1.739E6
8	Top Chain	220.0	0.160	449.5	2.070E6

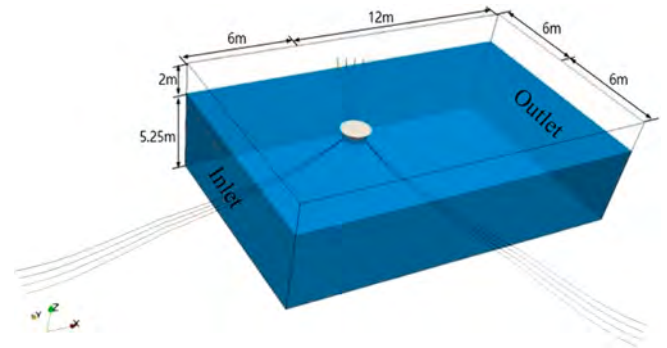


Fig. 4. Computational domain.

Table 3
Parameters in mesh convergence study.

Mesh	N_x	Δx (m)	Δy (m)	Δz (m)
Coarse	132800	0.128	0.14	0.04
Medium	1056000	0.064	0.07	0.02
Fine	3556800	0.042	0.047	0.0133

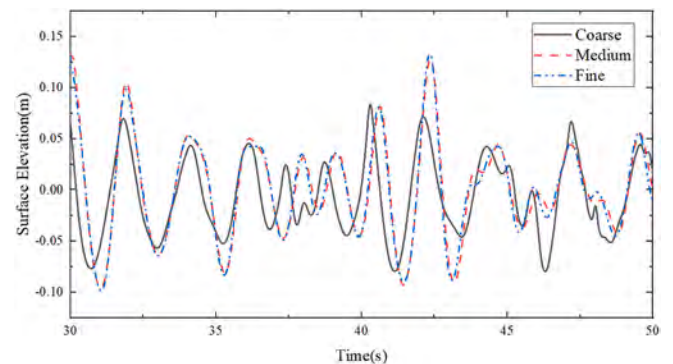


Fig. 5. Time series of surface elevation at origin.

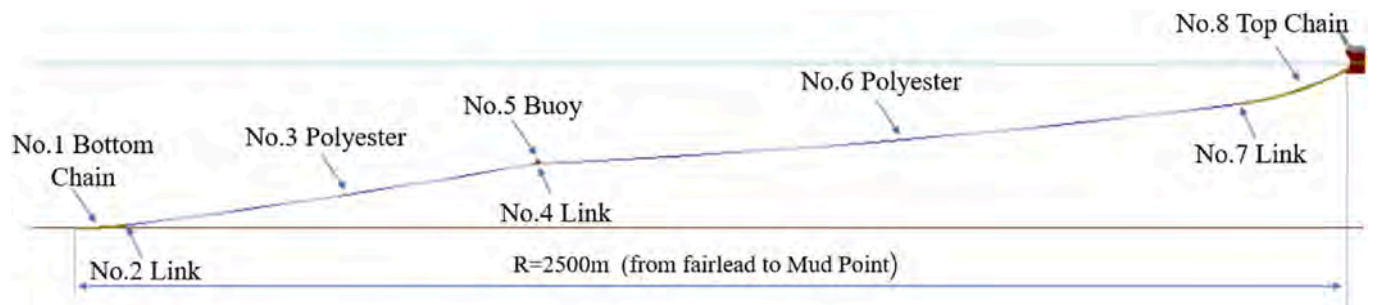
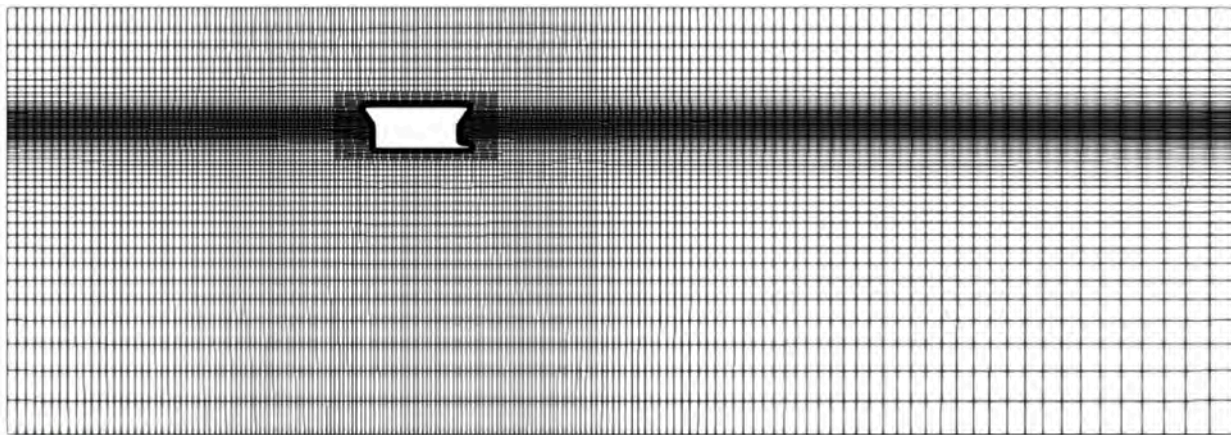
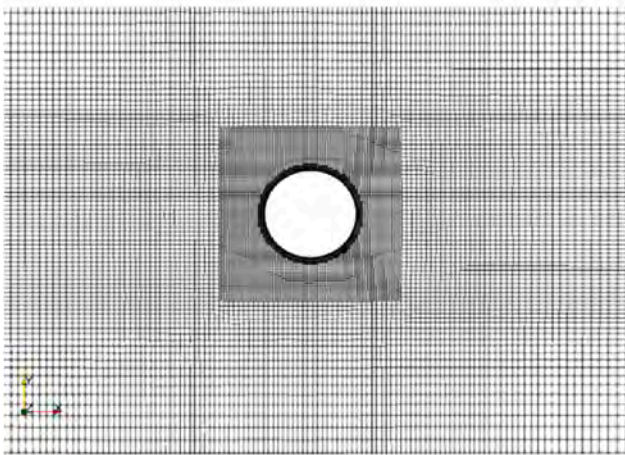


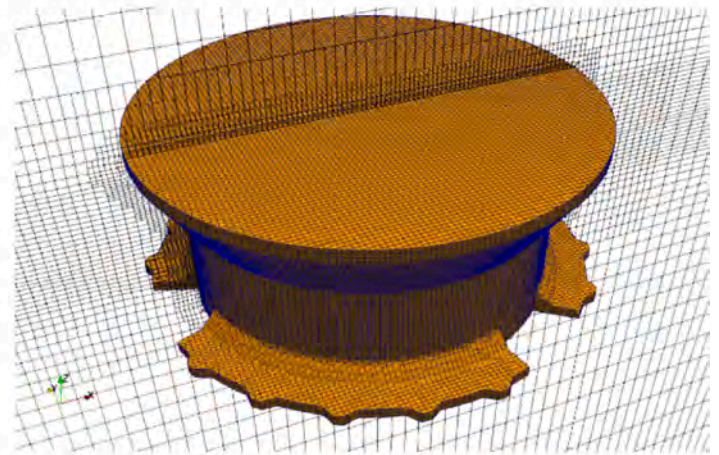
Fig. 3. Mooring line composition.



(a) Overview on x-z plane ($y = 0$)



(b) Magnified view on x-y plane ($z = 0$)



(c) Magnified view near CFPSO

Fig. 6. Computational mesh.

Table 4

Typical load conditions in model test (Deng et al., 2022b).

Case	Draft(m)	Wave $H_{1/3}$ (m)	Wave T_p (s)	Wave γ	Wave direction (deg)	Current Velocity (m/s)	Current Direction (deg)	Repeat
1	0.308	–	–	–	–	0.257	0	1
2	0.308	0.228	1.949	2.2	60	–	–	3
3	0.308	0.228	1.949	2.2	30	–	–	3
4	0.308	0.228	1.949	2.2	0	–	–	3
5	0.38	0.228	1.949	2.2	60	0.257	60	3
6	0.38	0.228	1.949	2.2	30	0.257	30	3
7	0.38	0.228	1.949	2.2	0	0.257	0	3
8	0.38	0.228	1.949	2.2	60	–	–	3
9	0.38	0.228	1.949	2.2	30	–	–	3
10	0.38	0.228	1.949	2.2	0	–	–	3
11	0.308	0.228	1.949	2.2	60	0.257	60	3
12	0.308	0.228	1.949	2.2	30	0.257	30	3
13	0.308	0.228	1.949	2.2	0	0.257	0	3

adopts the piecewise extrapolation method (PEM) (Liu and Wan, 2013). The composition of the mooring line in full scale is shown in Fig. 3 and Table 2.

3.3. Computational domain and mesh

The computational domain is illustrated in Fig. 4 using a Cartesian coordinate system. The coordinate origin of the frame is located at the center of the section where the water plane intersects the CFPSO. The

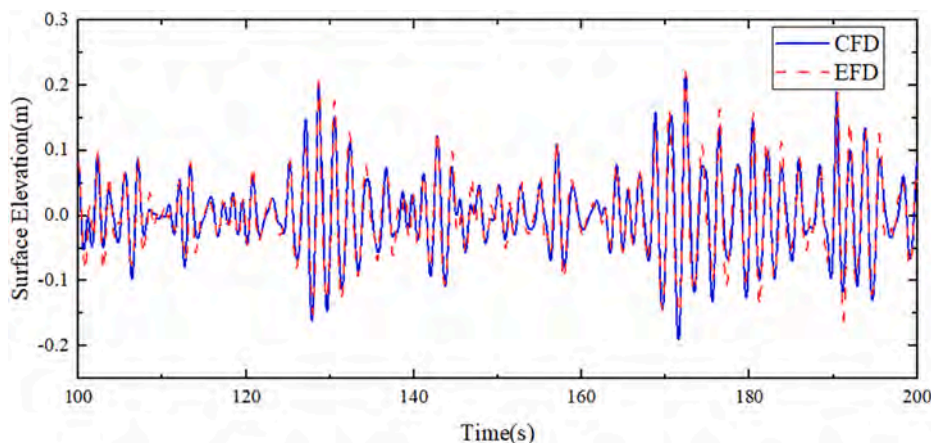


Fig. 7. Time series comparison of surface elevation at origin.

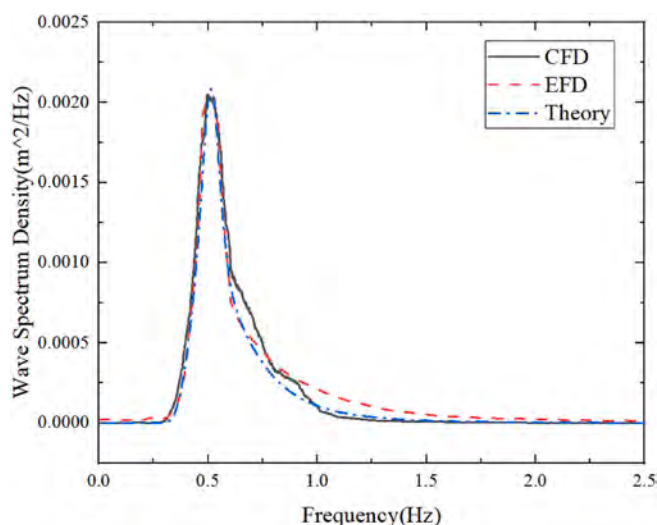


Fig. 8. Wave energy density comparison.

water depth of the computational domain is consistent with that of the physical experiment pool. The length of the computational domain can be appropriately shortened due to the implementation of the GABC method, which eliminates the need for a relaxation zone. The computational domain extends to: $-6 \leq x \leq 12$ m, $-6 \leq y \leq 6$ m, and $-5.25 \leq z \leq 2$ m (length \times width \times depth).

To ensure computational accuracy while minimizing simulation cost, it is necessary to verify the mesh convergence and determine an appropriate mesh size. In the mesh convergence verification, the surface elevation at the origin of the empty field without structures is investigated. The parameters of wave and current are consistent with those used in the model test, with the significant wave height of 0.228m, peak wave period of 1.949s and current velocity of 0.257 m/s. Three groups of meshes with different sizes (coarse, medium, and fine) are generated for convergence study, and the information of the three meshes are shown in Table 3. N_t is the total number of mesh cells. Δx , Δy and Δz respectively represent the length of the mesh in the direction of three coordinate axes near the origin.

Fig. 5 illustrates the time series of surface elevation at the origin. It can be seen that the results of the coarse mesh are significantly different from those of the medium mesh and the fine mesh, which can be seen in the attenuation of wave height, the difference of wave shape and the shift of wave phase. The results of medium mesh and fine mesh are very similar, and their time series are almost coincident, with only slight

differences in the case of lower wave heights. The above results show that the solution converges with the mesh refinement.

Medium mesh is used as the background mesh generated by *block-Mesh*, which will be refined in subsequent steps. To ensure the slenderness ratio of the body-fitted mesh, the *topoSet* tool is used to select a box. The box domain is set to: $-1.2 \leq x \leq 1.2$ m, $-1.2 \leq y \leq 1.2$ m, and $-0.58 \leq z \leq 0.57$ m. Within the box domain, the cells in the x-direction and y-direction are refined in one level. The z-direction grid remains unchanged. Within the range of 0.1m from CFPSO, the cells are refined in second levels. In order to analyze the flow separation and wake vortex structure of the CFPSO under the combined wave-current condition, it is necessary to set a boundary layer on the surface of the CFPSO. The thickness of the first layer boundary mesh is 0.003m, which ensures that the y^+ is around 40 and meets the requirements of wall functions. Finally, the total number of grid cells is 2.8 million. The mesh is shown in Fig. 6.

3.4. Boundary conditions and numerical schemes

The inlet and outlet of the computational domain are set to GABC boundary conditions to complete wave generation and wave absorption, while the left and right are set to symmetry plane, thus removing the limitation of computational domain width on numerical simulation. No-slip boundary conditions are used for the bottom and CFPSO surfaces.

Numerical simulations are carried out in the framework of the finite volume method. The Crank–Nicolson scheme is selected for the time discrete format. According to the research of scholars, when the mixing coefficient is set to 0.95, the simulation efficiency and simulation effect can be satisfied at the same time (Zhuang and Wan, 2021). In the momentum equation, both the convection term and the diffusion term are discretized by the second order accurate discretization method. In order to ensure the accuracy of the solution of the liquid-gas interface, the transport equation of the volume fraction is discretized by the *Gauss interfaceCompression vanLeer* method. The solution of the velocity field and the pressure field adopts the PIMPLE algorithm which combines the PISO algorithm and the SIMPLE algorithm. To ensure that the Courant number in the simulation domain is always below 1, the simulation time step is selected as 0.005s.

3.5. Case condition and wave calibration

The CFPSO studied in this paper operates in the South China Sea, which has relatively rough sea states. The wave spectrum in the South China Sea has a similar shape to the JONSWAP spectrum, which has a single spectral peak with a narrow average frequency width (Hasselmann et al., 1980). Therefore, the JONSWAP wave spectrum with constant flow velocity is selected for both numerical simulation and model

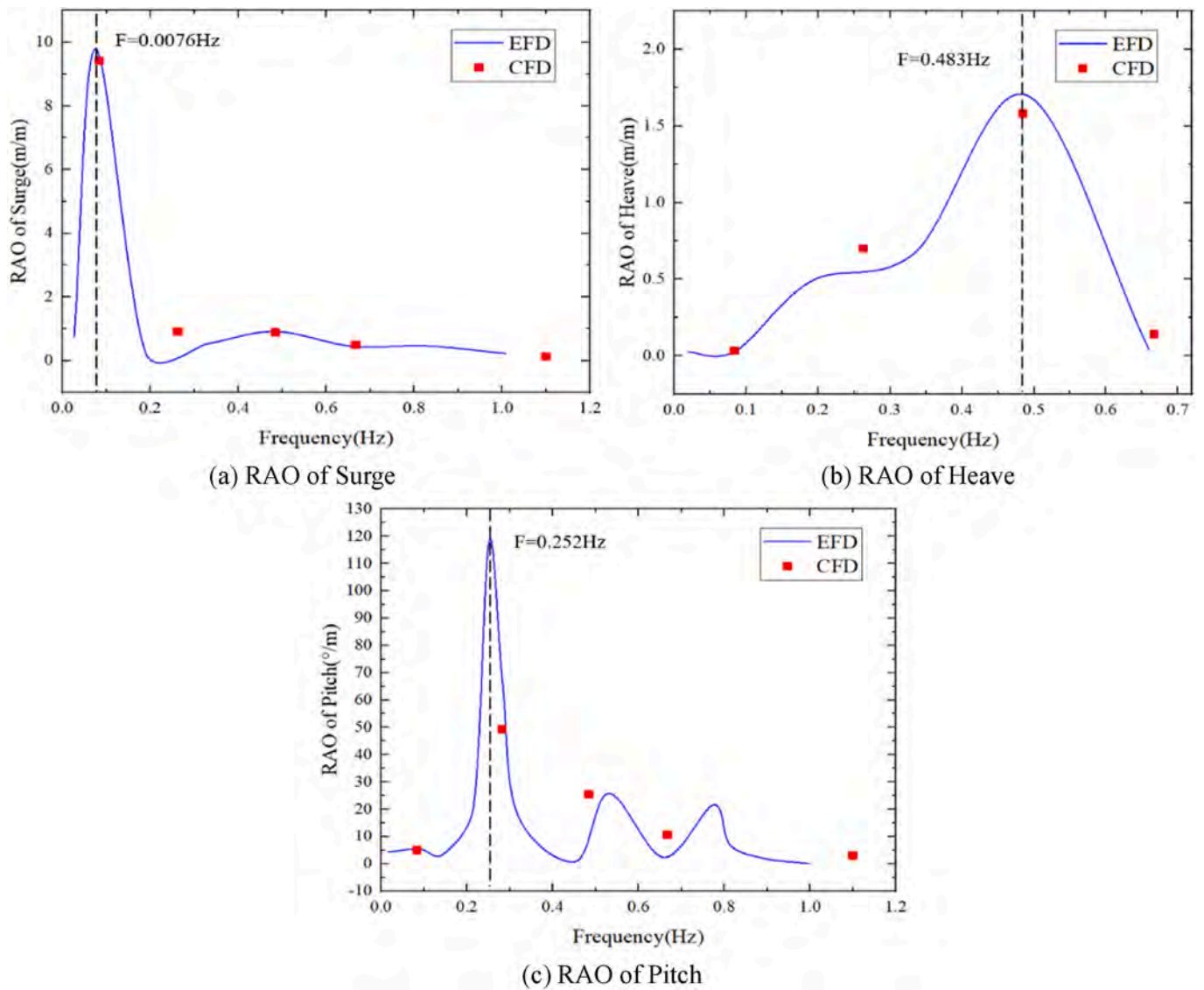


Fig. 9. RAO of the surge, heave and pitch motions.

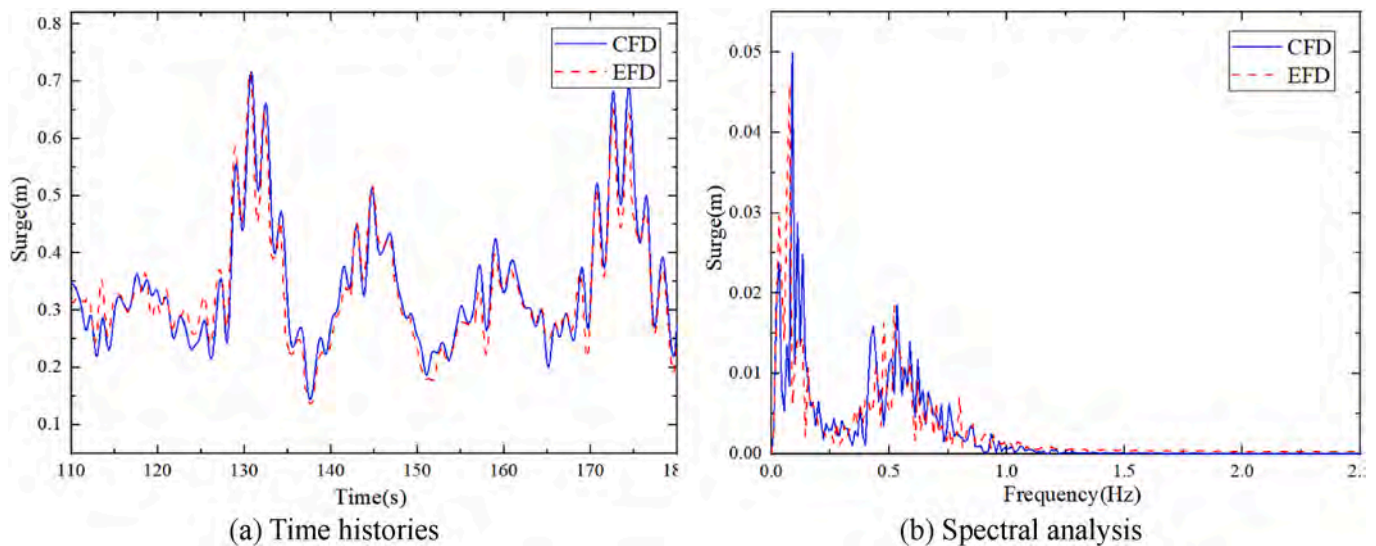


Fig. 10. Surge of the CFPSO in combined irregular wave and current.

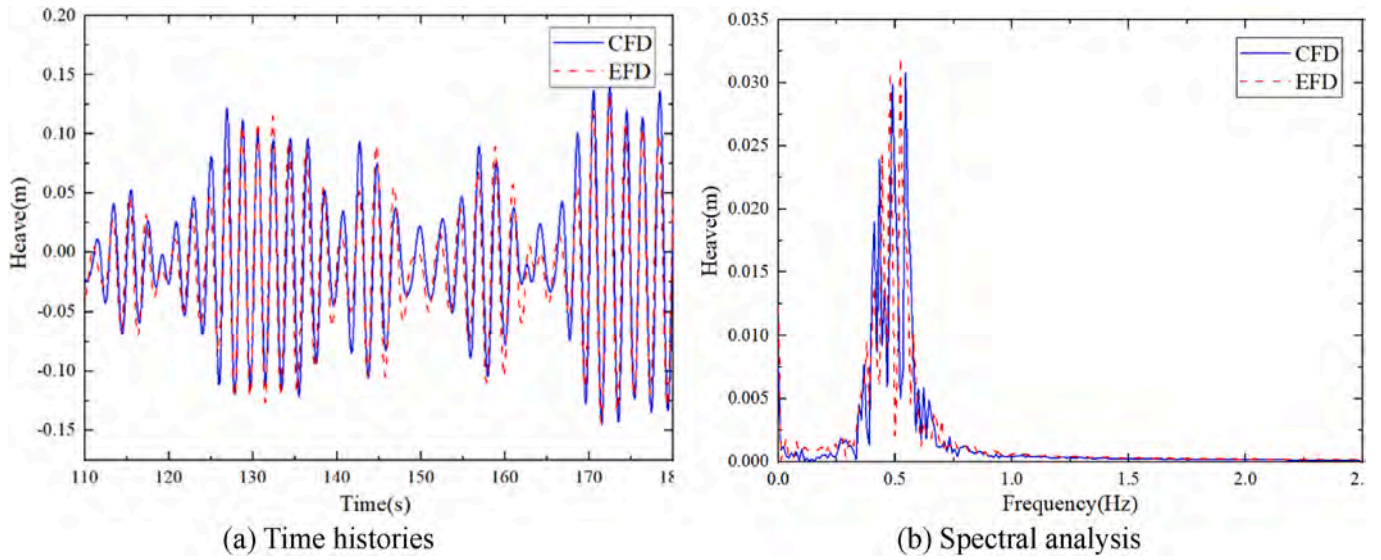


Fig. 11. Heave of the CFPSO in combined irregular wave and current.

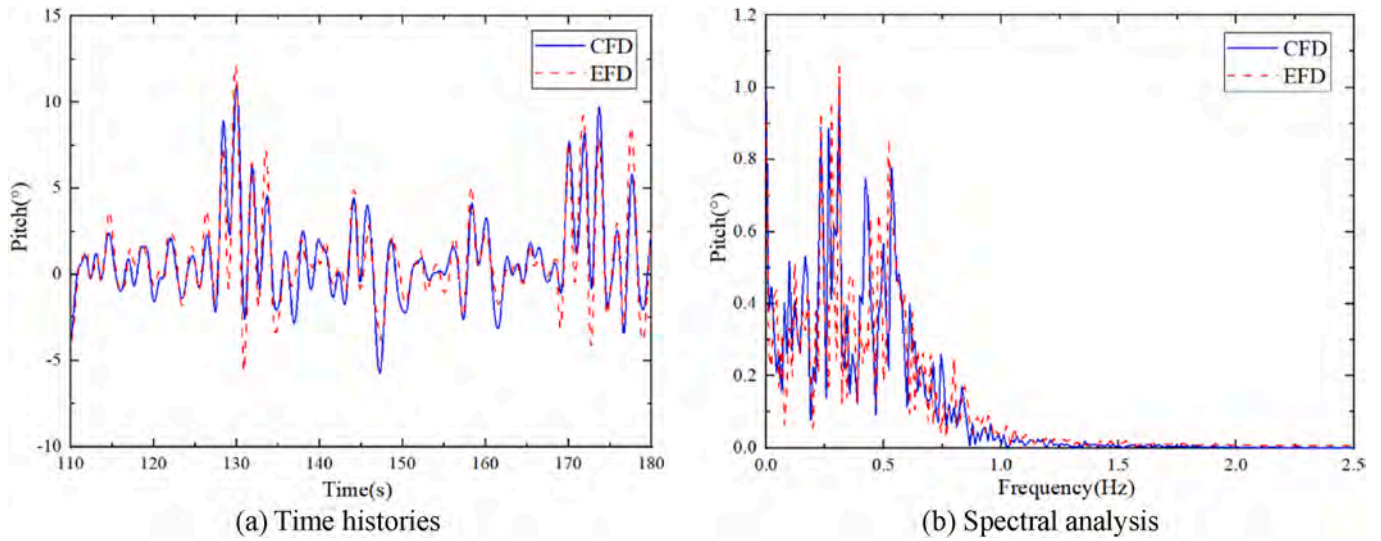


Fig. 12. Pitch of the CFPSO in combined irregular wave and current.

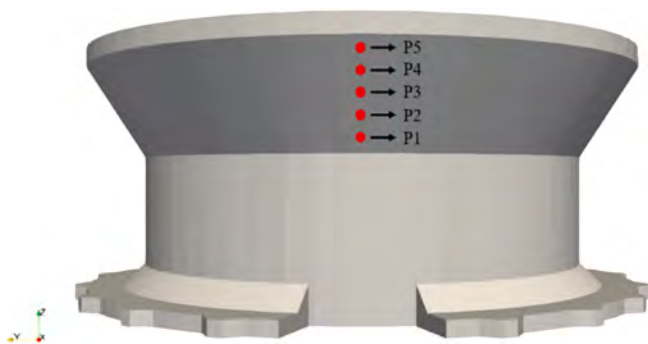


Fig. 13. Sketch of pressure probes on the CFPSO hull.

Table 5
Coordinates of pressure probes.

Pressure probes	x(m)	y(m)	z(m)
P1	-0.6209	0	0.0556
P2	-0.6478	0	0.1002
P3	-0.6745	0	0.1448
P4	-0.7014	0	0.1894
P5	-0.7283	0	0.2338

test. The wave energy density expression of the JONSWAP wave spectrum is as follows:

$$S(\omega) = 319.34 \frac{H_{1/3}^2}{T_p^4 \omega^5} \exp \left[-\frac{1948}{(T_p \omega)^4} \right] \gamma \exp \left[\frac{-(0.159 T_p \omega - 1)^2}{2\sigma^2} \right], \quad (13)$$

$$\sigma = \begin{cases} 0.07 & \text{if } \omega \leq \omega_p \\ 0.09 & \text{if } \omega > \omega_p \end{cases}, \quad (14)$$

where $H_{1/3}$ is the significant wave height, T_p is the period of the spectral

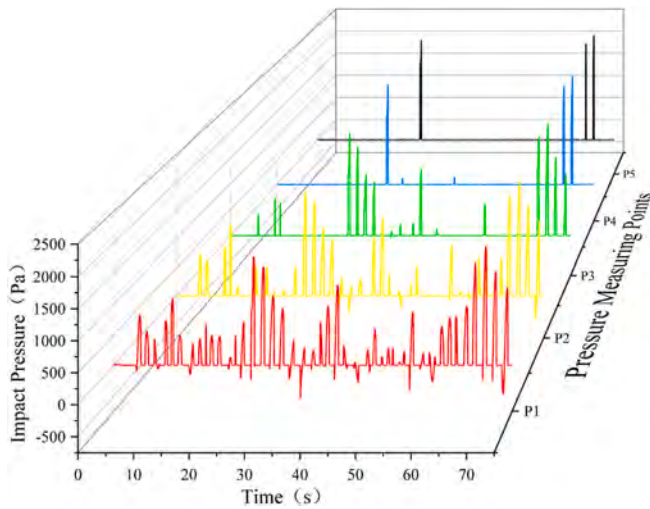


Fig. 14. Time histories of impact pressure at different pressure probes.

peak, ω_p is the frequency of the spectral peak.

The model test was carried out by Offshore Oil Engineering Co., Ltd (Deng et al., 2022b) in the deep-water wave basin of Shanghai Jiao Tong University (SJTU). Table 4 shows the typical load conditions in scaling model test.

In the present numerical simulation, we choose the condition of 0-degree wave and current direction under full load state, which corresponds to case 7 in Table 4.

In the numerical simulation process, in order to ensure that the surface elevation time series at the origin is consistent with the results of the model test, we extract the surface elevation time series at the position 6m in front of the CFPSO (the entrance of the numerical simulation domain) from the test results. A Fast Fourier transform (FFT) processing is performed to get the frequency, amplitude and phase of each wave components, which were later used for the irregular wave generation.

To ensure the accuracy of the generated numerical wave and current, it is necessary to calibrate the wave surface elevation at the origin of the computational domain. To save the simulation time, the numerical wave calibration is performed on a two-dimensional computational domain without floating object. During wave calibration, the input wave parameters are iteratively modified by measuring the wave information at the origin of the numerical domain. After several iterations, the numerical wave at the origin is able to be consistent with the wave in model test.

The comparison of wave surface elevation from CFD and EFD at the origin shown in Fig. 7 correspond very well. We also perform FFT on the wave surface elevation within 500s–1500s to obtain the corresponding wave amplitude at each frequency, and use equation (15) to convert the wave amplitude into wave energy density. The “smooth” function (Guinón et al., 2007) in MATLAB is used to smooth the wave energy density spectrum curve, the smoothing method being selected as “moving”, and the smoothing parameter “span” being selected as “99”. Fig. 8 shows the comparison of the wave energy density curve at the origin obtained from numerical simulation with the model test results and theoretical values. It can be seen that the numerical simulation results are in good agreement with model test and theory. The results shown in Figs. 7 and 8 prove that the accuracy of the numerical method used in this paper is reliable.

$$S(\omega) = \frac{A(\omega)^2}{2\Delta\omega} \quad (15)$$

where, ω is the circular frequency, A is the wave amplitude at the corresponding circular frequency. $\Delta\omega$ is the sampling interval of circular frequency.

4. Results and discussions

4.1. Motion response

Since the geometry of the CFPSO and the mooring configuration are symmetrically distributed along the propagation direction of the wave flow, the amplitudes of sway, roll and yaw motion are very small in both experimental and numerical results. Therefore, the motion in the above three degrees of freedom is not analyzed in this paper.

Before discussing the motion characteristics of the CFPSO in combined wave-current flows, its motion RAO in wave is given first. Fig. 9 shows the RAO of surge, heave, and pitch obtained from model tests and numerical simulations. The EFD results are from white noise test, and the CFD results are from regular wave simulations. The figure shows that the CFD results are in good agreement with the EFD results, and the mooring system has little effect on the natural frequencies of the heave and pitch motions of the CFPSO. In addition, the natural frequency of surge motion is very small, at only 0.0076Hz. This is due to the mooring system having less restoring force in the horizontal direction, and the water also providing less resistance to the CFPSO in that direction.

Fig. 10, Figs. 11 and 12 show the time series and FFT curves of surge, heave and pitch of the CFPSO under the combined irregular wave-current flow. In the figures, the blue solid line represents the numerical simulation result and the red dotted line represents the model test result.

The time series results indicate that the CFD results are in good agreement with the EFD results, with only a slight error observed in small pitch motion. The error is due to a slight difference in the center rotation of the CFPSO in the model test versus the numerical simulation. Due to the impetus of the water flow, the mean value of the surge motion deviates from the origin 0.34m and the mean value of the pitch motion deviates from the origin 0.92°. The maximum oscillation amplitude is also quantitatively analyzed. In heave motion, the maximum oscillation amplitude obtained by the model test is 0.131m, while the result obtained by the numerical simulation is 0.138m, with the error of 5.3%. Similarly, the surge error is 9.8%, and the pitch error is 8.7%. It can be seen that the errors of the time-history curves of the three degrees of freedom are not more than 10%.

The spectral analysis results also demonstrate good agreement between the CFD and EFD results. Figures are not smoothed using the smoothing function in spectral analysis, as this may ignore detailed features. For the surge and pitch motion, one main peak and one sub-main peak can be clearly seen in the figures, indicating that the CFPSO is excited by the motion of the two components under the combined action of the wave and current. The main peak corresponds to its own natural motion frequency and the sub-main peak corresponds to the frequency corresponding to the wave spectrum peak period. For the heave motion, since the natural period of heave is relatively similar to the wave spectrum peak period, no clear main peak and sub-main peak phenomenon are observed. Only one peak corresponds to the frequency corresponding to the wave spectrum peak period. The CFD results is always slightly larger than the EFD results, whether for the frequency corresponding to the main peak or the sub-main peak. However, the error is within 5%. This may be due to the inaccuracy of the wave calibration and the difference between the numerical mooring and the model test mooring. The surge motion with a very large amplitude is excited at the CFPSO surge natural frequency of 0.0076 Hz, even though the wave energy density of this frequency is very small. This is due to the fact that under the action of current, the equilibrium position of surge motion is not at the origin, resulting in a second-order wave drift force. The frequency of the second-order force is close to the surge nature frequency of the CFPSO, inducing the simple harmonic motion of surge and causing a significant surge motion of the CFPSO. Similarly, because the action point of the force generated by the flow is not on the rotation center of the CFPSO, the pitch equilibrium position of the CFPSO also changes, generating a low-frequency moment that excites the pitch

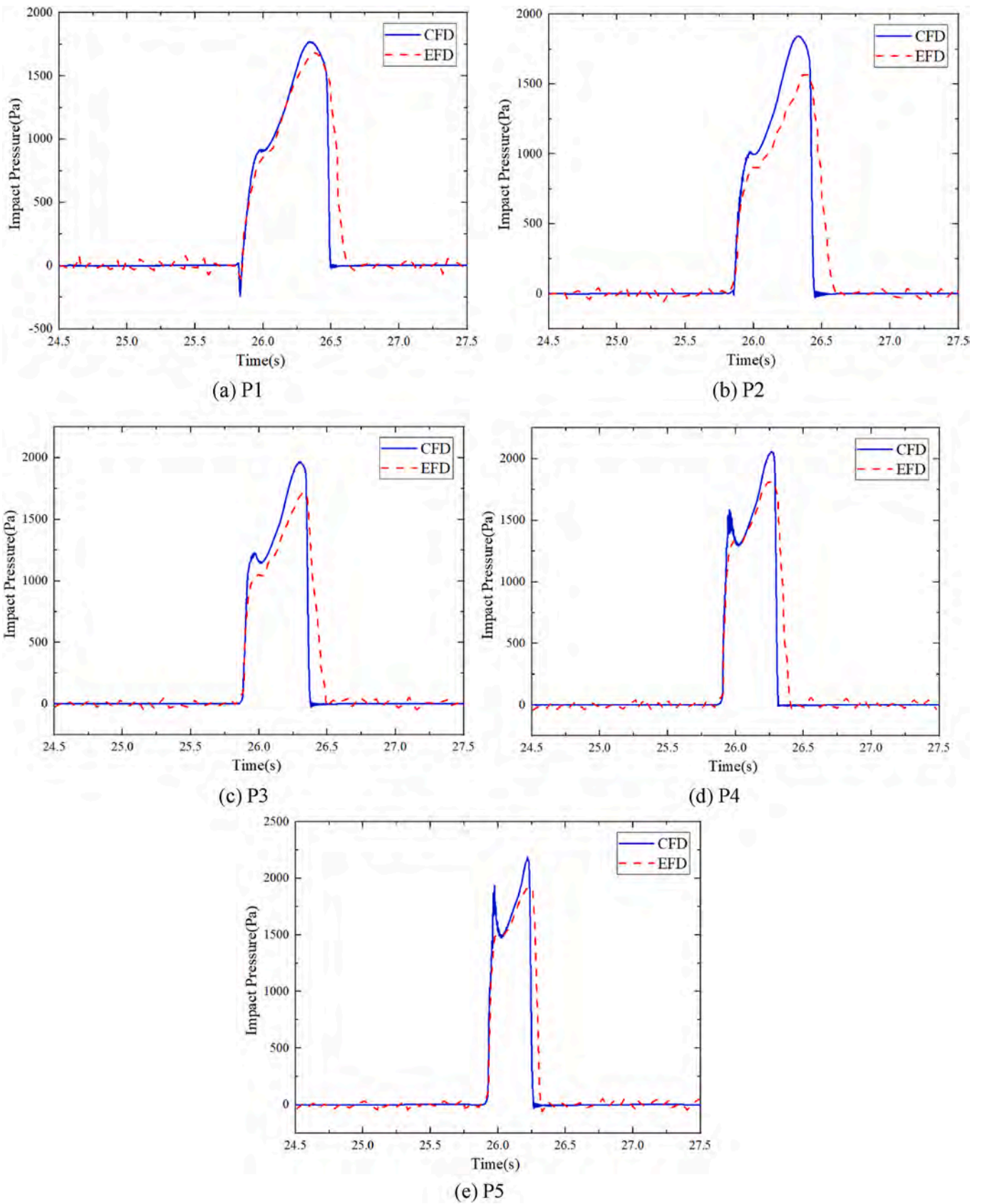


Fig. 15. Impact pressure of different pressure probes during one typical slamming event.

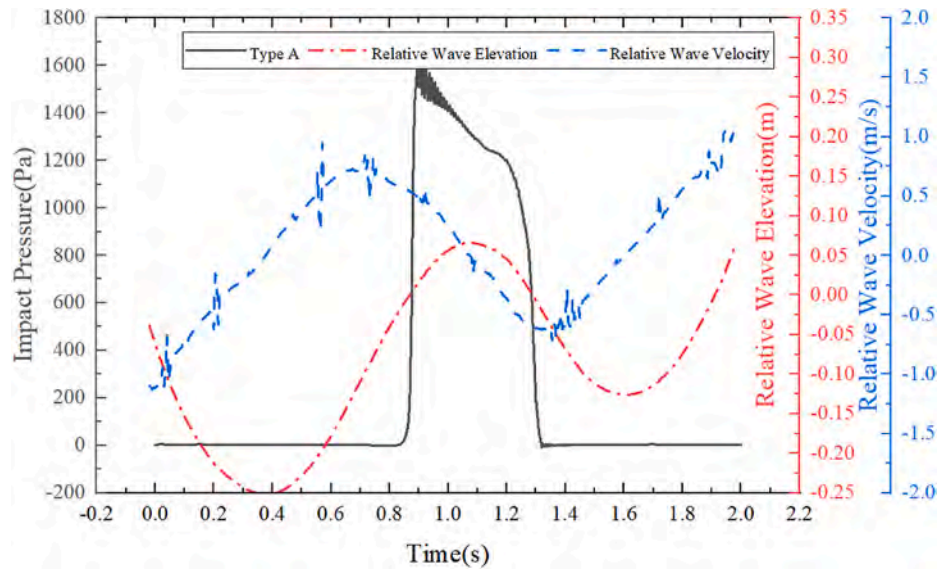


Fig. 16. Impact pressure, relative wave elevation and relative wave velocity time series during Type A slamming event.

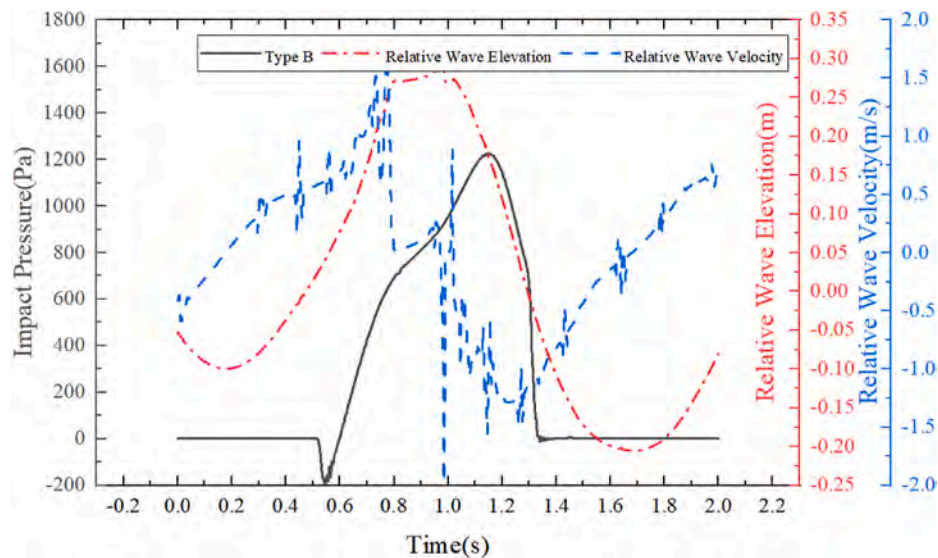


Fig. 17. Impact pressure, relative wave elevation and relative wave velocity time series during Type B slamming event.

motion of the CFPSO. However, the frequency of low-frequency moment is much smaller than the pitch natural frequency of CFPSO, so no obvious low-frequency pitch motion is excited.

4.2. Impact pressure

Five pressure probes are arranged at the mid longitudinal section of the wave-facing side of the CFPSO model, as shown in Fig. 13. The coordinates of pressure probes are listed in Table 5.

The waterfall chart in Fig. 14 shows the time series of the wave impact pressure of each pressure probe obtained by CFD method. It can be seen from the figure that the closer the pressure probe is to the waterline, the greater the number of monitored slamming and the longer the monitored slamming duration. The peak pressure of each probe is no obvious difference, all of which are about 2000pa. Negative slamming dynamic pressure can be observed at the pressure probes P1 and P2, which may be caused by the viscous fluid detaching from the surface of the hull.

In Fig. 15, the numerical results of one typical slamming event are

intercepted from each pressure probe, and compare with the test results. Due to the 20 kHz ultra-high frequency sampler used in the model test, a lot of noise exists in the original data, making it difficult to make comparison. Therefore, the smooth function is used to smooth the test data. By comparison, it can be seen that the numerical results of all the pressure probes are greater than the model test results. The maximum error is at P2, with the error about 20%. The numerical results of impact pressure action time at all the pressure probes are shorter than model test results, with the error not more than 20%. The impact pressure curve obtained by numerical simulation is relatively smooth, and the impact pressure curve obtained by experiment is relatively rough. The reasons for the above phenomenon may be the errors caused by data smoothing.

4.3. Correlation between relative wave elevations and relative wave velocities and impact pressure

A careful observation of the shape of impact pressure time histories shows that the shape of the curve formed by each slamming is not same,

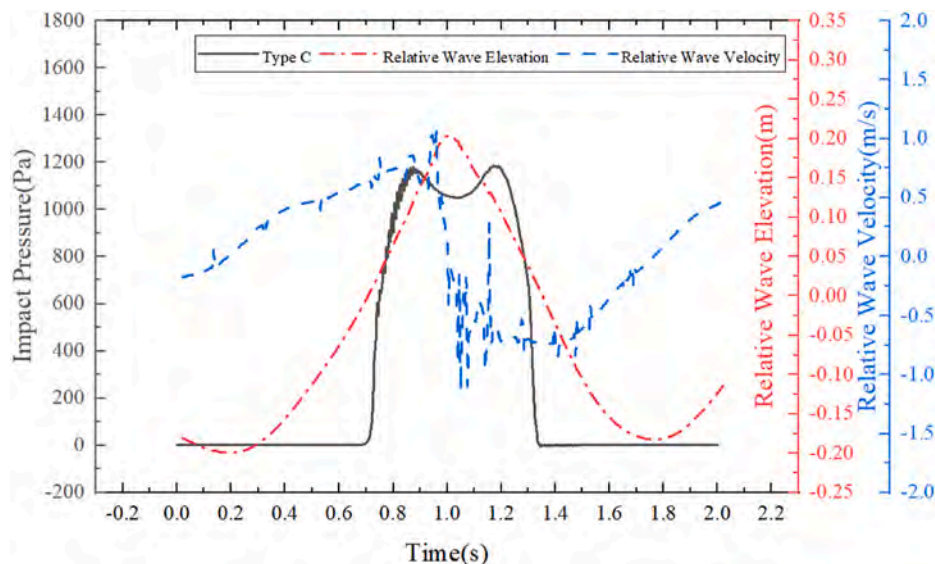


Fig. 18. Impact pressure, relative wave elevation and relative wave velocity time series during Type C slamming event.

different from the conclusion obtained from the slamming test of the fixed structure (Ha et al., 2019). We postulate that the aforementioned phenomenon could be attributed to the continual variations in relative wave height and velocity due to the motion of structures in waves (Buchner and Voogt, 2009). The relative wave elevation represents the distance between the probe and the wave surface. When the crest passes through the structure, a positive relative wave elevation indicates that the dynamic water pressure is greater when the value is smaller. The relative wave velocity reflects the degree of impact of the water flow on the structure. A positive value for relative wave velocity corresponds to higher dynamic water pressure when the value is larger. Therefore, wave slamming is a combined problem of relative wave elevations and relative wave velocities. In order to verify this conjecture, the time series formed by each slamming of the P1 pressure probe are roughly divided into three categories named Type A, Type B and Type C, according to the shape of the curves. As shown in Fig. 16, Figs. 17 and 18, we select one representative curve from each type and draw the slamming time series, the relative wave elevation curve and relative wave velocity curve in the same figure. For Type A curves, the impact pressure initially rises rapidly, followed by a slow decline, and then a rapid drop. For Type B curves, the impact pressure curve exhibits a rapid rise at first, followed by a slower rise and then a quick fall. For Type C curves, the impact pressure curve presents double peaks, and the slamming curve is symmetrical.

Combining the impact pressure curve with the relative wave elevation and velocity curves to analyze, whether it is Type A, Type B or Type C, When the slamming occurs, the relative wave elevation curve turns from negative to positive, and when the slamming ends, the relative wave elevation curve turns from positive to negative. For the Type A slamming event, the relative wave elevation maintains a small positive value at the start of the slamming, and the relative wave velocity is also positive, causing the impact pressure rising rapidly. As time progresses, although the relative wave elevation still maintains a small positive value, the relative wave velocity changes from positive to negative, leading to a small drop in impact pressure. For the type B slamming event, when slamming begins, the relative wave elevation increases rapidly, and the relative wave velocity reaches a peak of over 2 m/s. However, at this stage, the increase in relative wave elevation is due to the downward motion of the CFPSO, as the wave crest has not yet reached it. As a result, even though the relative wave elevation and velocity are relatively high, the slamming pressure curve only shows a slow upward trend. As time passes, the wave crest reaches the CFPSO. The relative wave elevation decreases and the probe approaches the

wave surface, resulting in a rapid increase in the impulsive pressure to its peak value. The characteristics of Type C slamming events are between Type A and Type B. At the position of the first peak of impact pressure curve, the influence of relative wave velocity on the impact pressure is dominant. At the position of the second peak, the influence of relative wave elevation on impact pressure dominates.

The slamming duration affects the fatigue life and durability of the CFPSO and the slamming peak pressure affects the strength and stability of the CFPSO. Type A slamming events are characterized by short durations and high peak pressures, while Type B slamming events have longer durations and lower peak pressures. Type C slamming events have characteristics that lie between Types A and B. All three types of slamming can cause structural damage to the CFPSO. Therefore, it is important to reduce the relative wave elevation and velocity when the wave crest arrives in order to decrease slamming pressure. The recommendations to CFPSO designers are: 1. Adjust the mass and inertia moment of CFPSO to make its heave natural frequency deviate from the peak frequency of the wave spectrum, reduce the amplitude of motion at the resonance frequency to reduce the wave elevation and velocity. 2. Optimize the structure of heave plate to reduce the movement amplitude of CFPSO in waves to reduce the wave elevation and velocity. 3. Add propulsion devices that can change the motion state of CFPSO, actively adjust the relative wave elevation and velocity under extreme sea conditions, change the phase difference between the motion and the wave to reduce the slamming pressure.

4.4. Flow field analysis

In this section, we analyzed the flow field around the hull and the heave plate, as well as in the wake region during a slamming event, aiming to explore the characteristics of the vortex structure evolution of the CFPSO under the combined wave-current coupling. Moreover, the streamline and surface pressure contour of one slamming event are given, and the change of impact pressure is analyzed from the perspective of flow field.

Fig. 19 shows the change of the vortex structure around the hull during the complete heave motion processes of the CFPSO. In the figure, “*t*” represents the time when CFPSO is located at a trough of the heave time histories and “*T*” represents the time required for CFPSO to move from “*t*” to the next trough position of the heave time series. The vortex structure in the figure is identified using the Q criterion (Hunt et al., 1988) and colored using the x-direction component of the vorticity field. Analysis of the figure shows that most of the vortices around the CFPSO

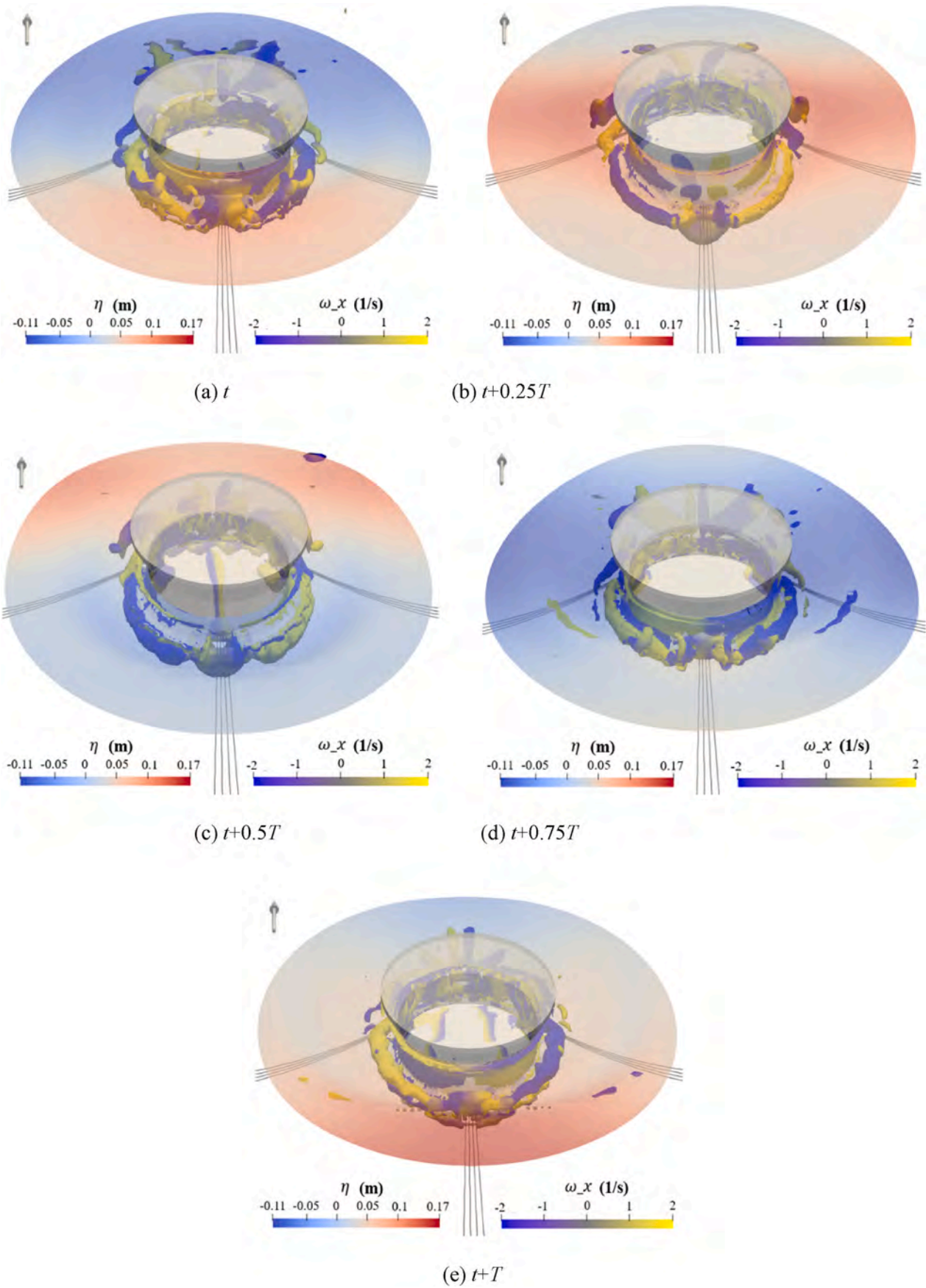


Fig. 19. Vortex structure around CFPSO.

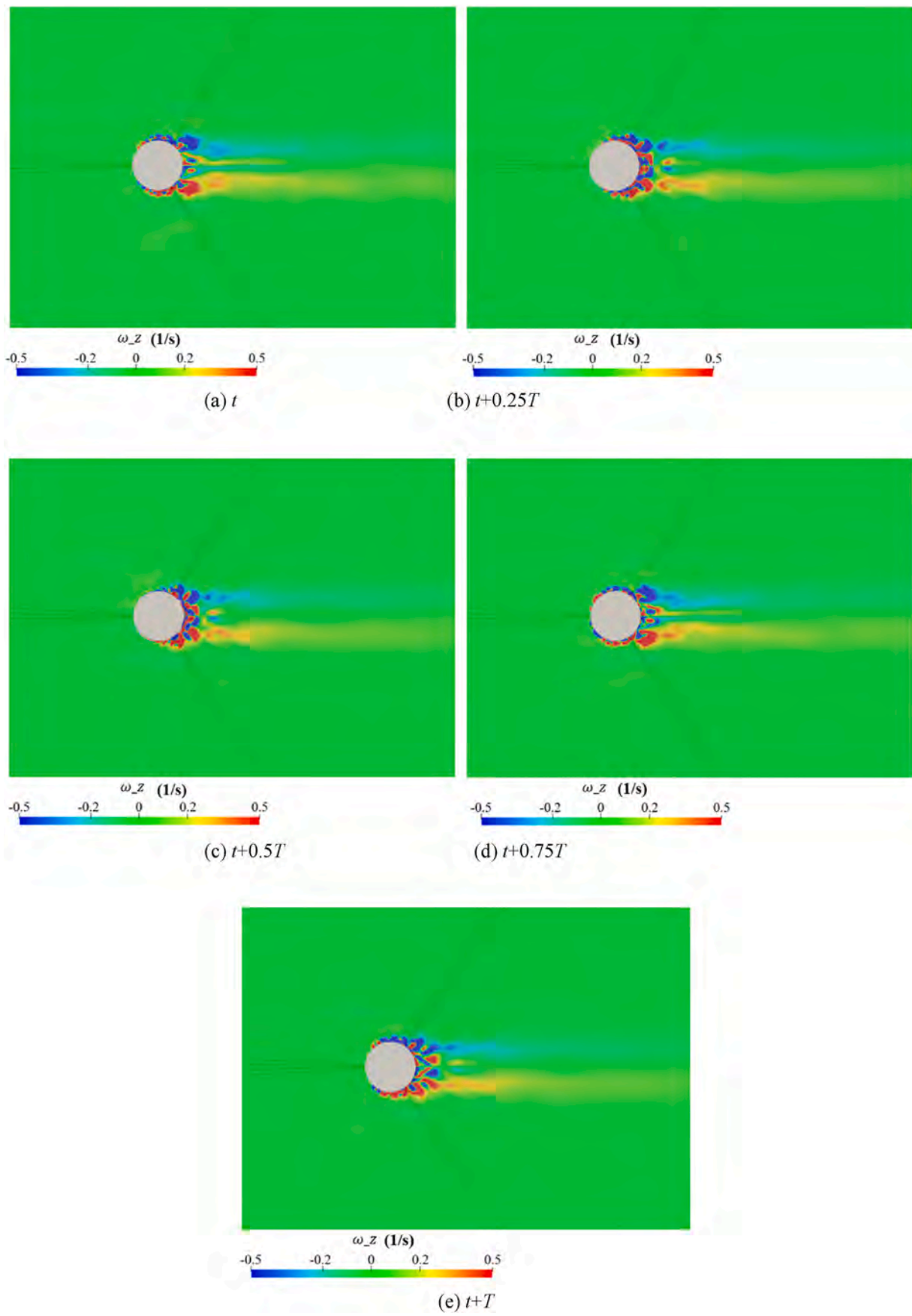


Fig. 20. Vorticity contour of CFPSO wake region.

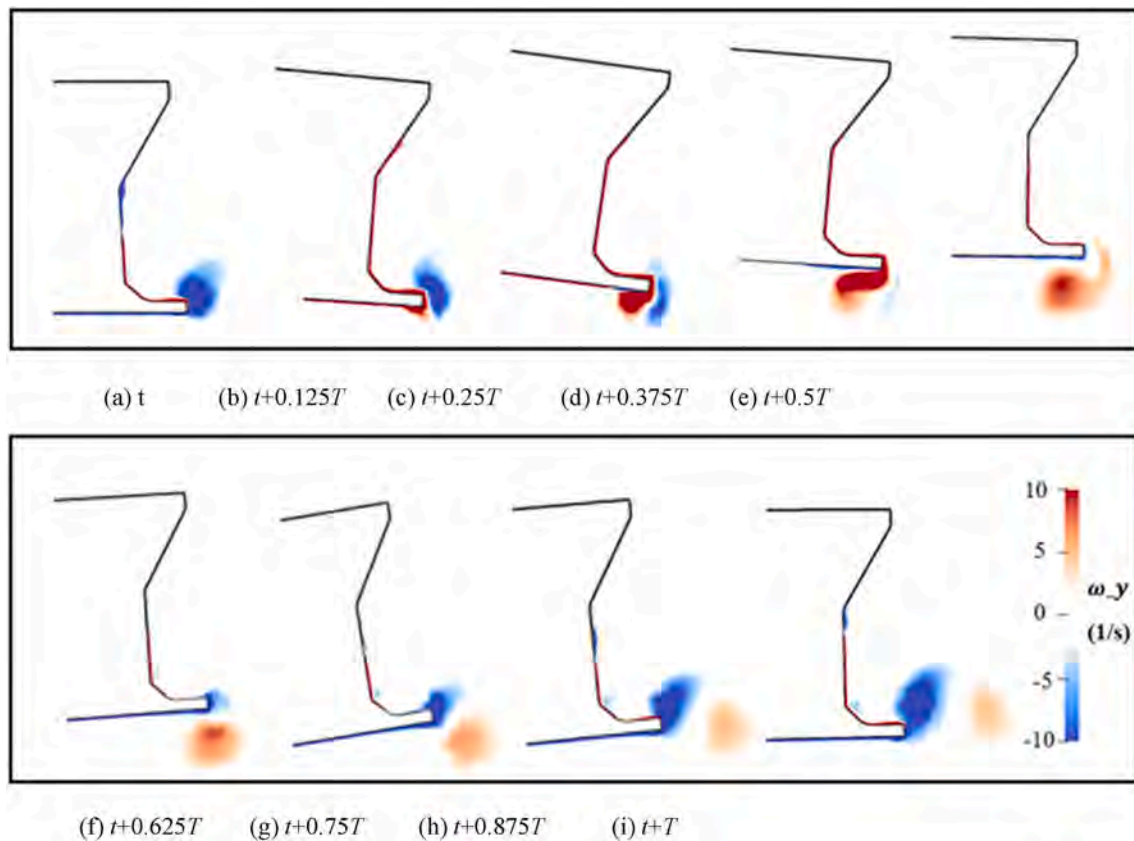


Fig. 21. Distribution of vorticity around heave plate.

are generated by the constant friction during the relative motion of the heave plate and the water. At the lowest point of the heave motion, oppositely flipped vortices are generated above the heave plate and continuously break away from it. As the CFPSO rises, the vortex above the heave plate gradually dissipates. When the CFPSO moves to the highest point, a vortex that flips in the opposite direction will be generated under the heave plate and separate from the heave plate. The above process repeats continuously in each motion cycle. Under the influence of the current, the wake region of CFPSO also forms a wake vortex due to the viscous pressure resistance, and the wake vortex and the vortex excited by the heave plate will move downstream and dissipate gradually with the drive of the current. In addition, during the continuous movement of CFPSO, the CFPSO and the water surface are constantly flapping, resulting in some small eddies at the intersection of the CFPSO and the water plane.

Fig. 20 shows the vorticity contour of the CFPSO wake region at the same time node as Fig. 19. Taking the z-axis as the normal and making a section 0.3m below the water plane, it can be observed that many small vortices with opposite rotation directions are generated near the conical protrusion of the heave plate during the continuous motion of CFPSO. The existence of these small vortices greatly increases the additional mass in the heaving direction of the CFPSO and can effectively reduce its heave amplitude. The flow velocity is 0.257 m/s, and the Reynolds number of the flow around the hull is 3.12×10^5 . The Reynolds number is just located in the critical region of the flow around the hull, where the vortex shedding is irregular and random (Yeon et al., 2016). Due to the influence of the wave and the motion of the CFPSO, there is no Karman vortex street in the wake region, and the vortices form two symmetrically distributed wakes that are quickly dissipated.

Fig. 21 shows the local vorticity distribution of the heave plate in the wake region of the CFPSO during one motion cycle. In the figure, the meanings of “ t ” and “ T ” have the same meanings as in Figs. 19 and 20. As the CFPSO rises from the lowest position and undergoes positive

pitching, the negative vortex initially located above the heave plate is eliminated, and a positive vortex is generated below the heave plate and close to the side of the hull. As the CFPSO moves to the highest point, the positive vortex detaches from the heave plate. After that, as the CFPSO continuously descends and pitches in the negative direction, a negative vortex is generated on the side of the heave plate away from the hull. This negative vortex also counteracts the positive vortex generated earlier. In the motion process of the CFPSO, the vortices can consume a significant amount of energy, thereby reducing the motion amplitude of the CFPSO.

As mentioned above, under the coupling effect of relative wave elevation and relative wave velocity, the impact pressure curve of probe P1 presents three different types. To provide a detailed illustration of the local flow of the flow field during slamming, Fig. 22, Figs. 23 and 24, respectively show the streamline and dynamic pressure contour in front of the CFPSO during a complete slamming process of the three slamming types of Type A, Type B and Type C.

Fig. 22 shows the complete Type A slamming event from 171.1s to 171.9s. The figures of 171.1s, 171.2s and 171.3s show the flow field before the slamming occurs. At this point, the probe P1 has not touched the wave surface, so the slamming dynamic pressure is zero. It can be seen from the figures of 171.4s and 171.5s that the streamlines at probe P1 change from sparse to dense within 0.1s, which indicates that the hull is squeezed by water. Besides, From the dynamic pressure contour that the maximum dynamic pressure is located on the wave surface, and as the relative wave elevation increases, the dynamic pressure decreases. The impact pressure reaches the maximum at this time due to the dual effects of water squeezing and small relative wave elevation. As shown in the figures of 171.6s and 171.7s, the streamlines at probe P1 change from dense to sparse, indicating that the tendency of water to squeeze the hull is reduced. This phenomenon is shown in Fig. 16 as a decrease in relative wave velocity. As shown in the figures of 171.8s and 171.9s, with the passage of the wave, the pressure probe is separated from the

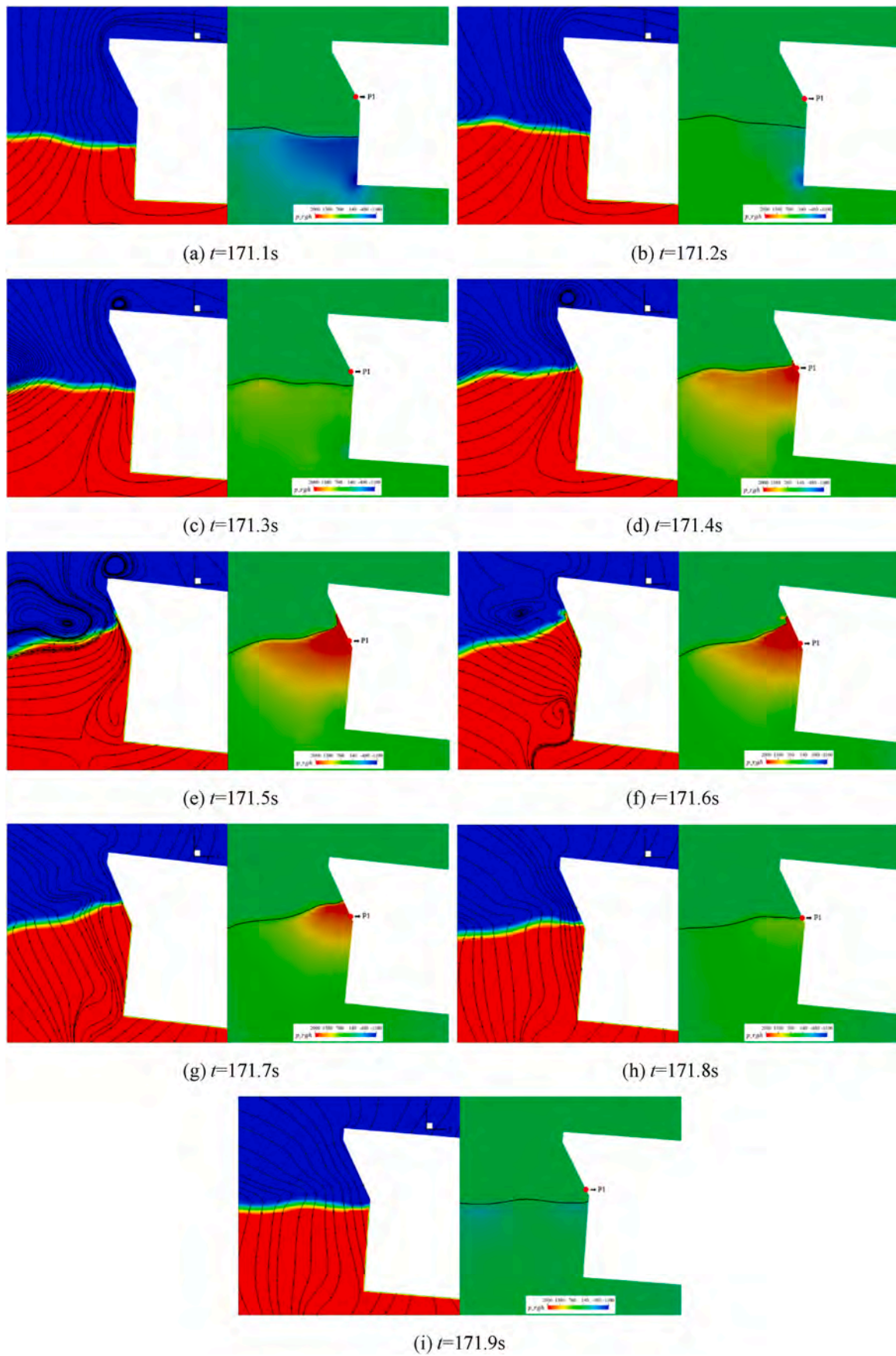


Fig. 22. Local streamline and impact pressure contour of Type A slamming event.

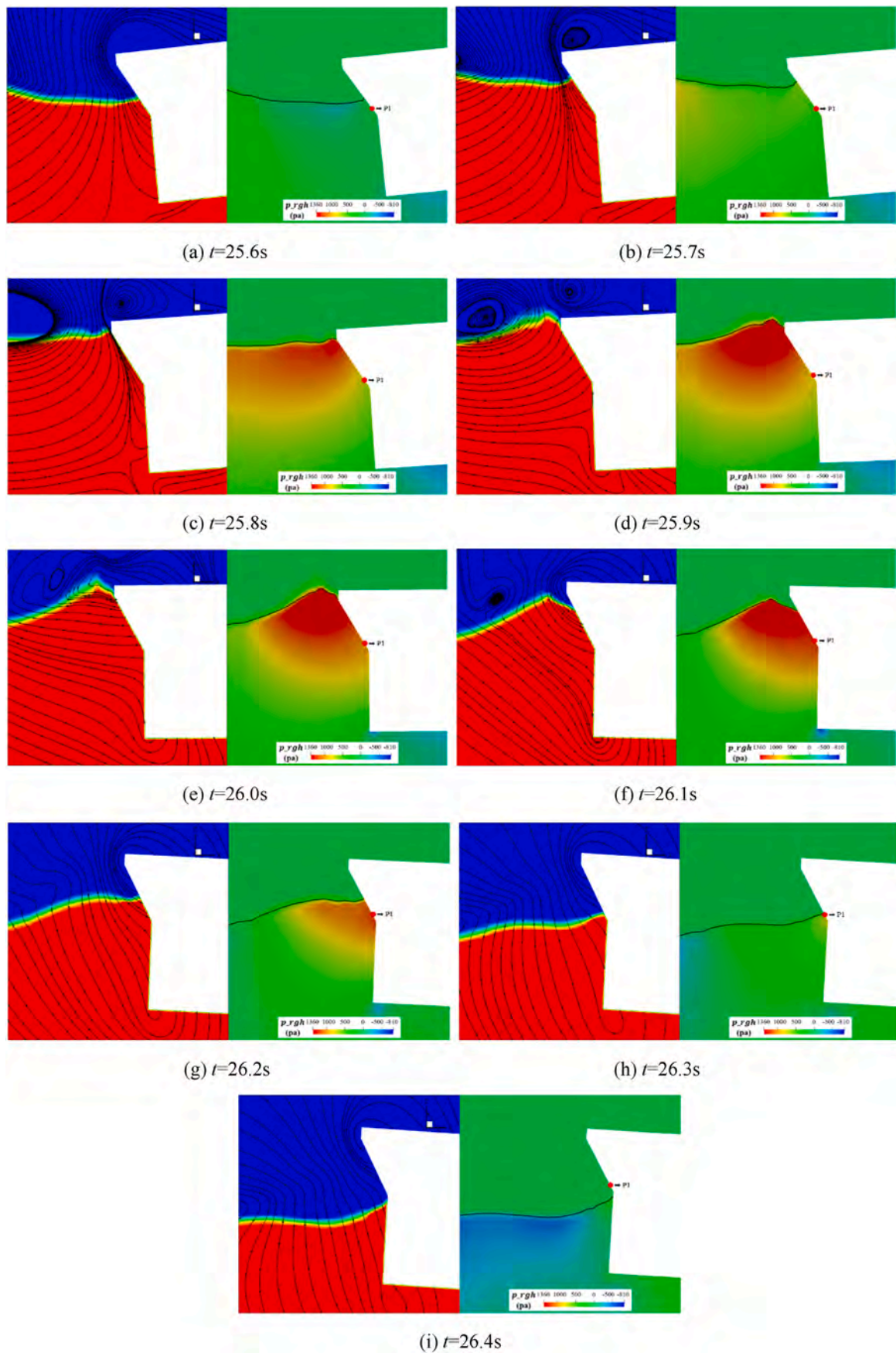


Fig. 23. Local streamline and impact pressure contour of Type B slamming event.

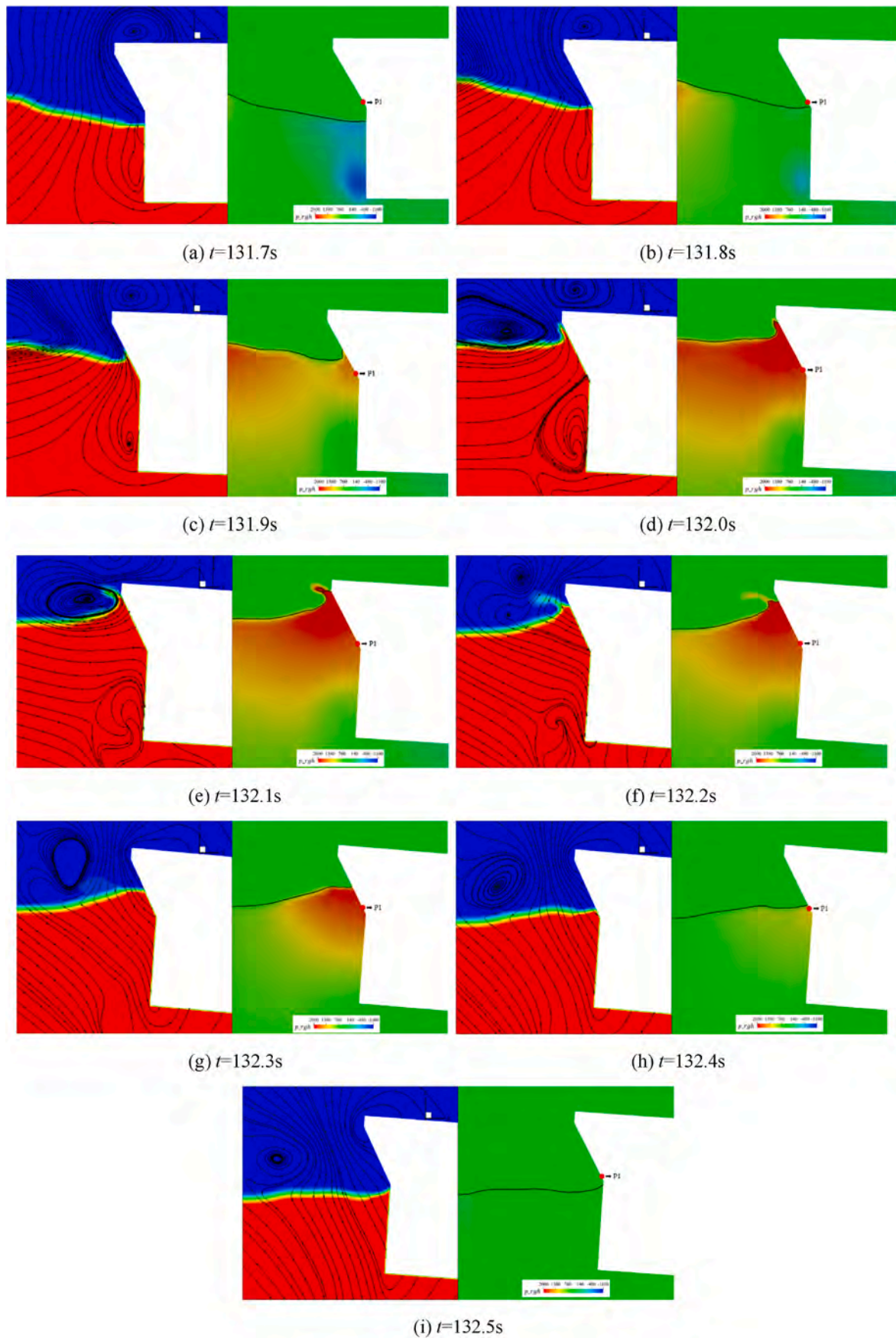


Fig. 24. Local streamline and impact pressure contour of Type C slamming event.

water surface, and the dynamic pressure drops to zero rapidly.

Fig. 23 shows the complete Type B slamming event from 25.6s to 26.4s. The figures of 25.6s and 25.7s show the flow field streamlines before the arrival of the wave. At this point, the CFPSO is located in the wave trough, and the streamline at the probe P1 on the CFPSO has an outward trend along the hull surface, indicating that the influence of the reverse velocity of the wave is greater than that of the uniform flow velocity. The water has a tendency to move away from the hull surface, resulting in negative dynamic pressure. This also proves that the negative value of the impact pressure in the Type B curve is reasonable. In the figure of 25.8s, the streamline around the CFPSO is nearly parallel to the hull of the CFPSO, indicating that the fluid neither tends to leave nor squeeze. This moment can be regarded as a turning point for the impact pressure from negative to positive. As shown in the figures of 25.9s–26.2s, with the approach of the wave crest, the streamline at the pressure probe shows an inward trend along the surface of the hull. At this point, the surface of the hull is squeezed by the water flow, resulting in significant impact pressure. As the wave lifts the CFPSO continuously, the pressure probe gets closer to the water surface and the relative elevation decreases, which further increases the impact pressure. These phenomena are consistent with the Type B curve shown in Fig. 17. In the figures of 26.3s and 26.4s, as the wave crest passes, the CFPSO further increases because the motion phase of CFPSO lags behind wave phase. When the pressure probe is separated from the water surface, the impact pressure rapidly drops to zero.

Fig. 24 shows the complete Type C slamming event from 131.7s to 132.5s. The figures of 131.7s, 131.8s and 131.9s show the flow field before slamming, with streamlines parallel to the hull and zero dynamic pressure at probe P1. In the figures of 132.0s, 132.1s and 132.2s, the streamlines point to the inside of the hull, resulting in a sharp rise of the relative wave velocity and the impact pressure. During 132.0s–132.1s, the CFPSO is descending, leading to a deeper draft at the probe, higher relative wave elevation, and lower dynamic pressure. During 132.1s–132.2s, the CFPSO is rising, resulting in a smaller relative wave elevation at probe P1 and higher dynamic pressure. This analysis supports the double peaked characteristic in Fig. 18. As shown in the figures of 132.3s, 132.4s and 132.5s, as the wave passes, the probe separates from the water surface, and the dynamic pressure drops to zero rapidly.

5. Conclusions

This paper proposes a new numerical approach for predicting the motion and slamming impact of CFPSOs in combined wave-current conditions. The proposed approach combines GABC method, buoyancy-modified k - ω SST turbulence model, and a self-developed 6DOF rigid body motion module. Motion response and wave slamming characteristics of the CFPSO under the combined action of irregular wave and current are investigated. The following conclusions can be drawn.

1. By performing wave calibration, the wave conditions for model test can be reproduced in numerical simulation. The predicted motion responses of CFPSO are in good agreement with the model test. The peak frequencies of surge, heave and pitch motions are the same with experimental data, and the errors of corresponding amplitudes at peak frequencies are less than 10%.
2. Three different types of slamming events are identified. Type A is characterized by a short duration and a "fast rise and slow drop" pattern. Type B is characterized by a long duration and a "slow rise and fast drop" pattern. Type C falls between the other two types and is characterized by "double peaks". These different types of slamming events are caused by the combined effects of relative wave elevation, relative wave velocity, and the motion of the CFPSO itself.
3. The Q criterion is used to extract the vortex structures around the CFPSO. Owing to the heave plates impeding heave motion, the vortex is mainly generated at the upper and lower edges of the heave

plates. The conical structures on heave plates can create multiple fine vortices, which may better restrain heave motion. Under the action of current, additional vortices form at the front, bottom and wake region of the CFPSO, which may cause the difference between the motion response of CFPSO under combined wave-current and that of CFPSO in wave only field.

In the future, based on the above study, we will consider the motion response difference of CFPSOs under combined wave-current conditions versus wave only conditions. And we will analyze the reasons for the difference from the perspective of the flow field.

CRediT authorship contribution statement

Shuaiwen Huo: Data curation, Writing – original draft, preparation, Visualization, Investigation, Software, Validation. **Shi Deng:** Data curation, Visualization, Investigation, Validation. **Zhengrong Song:** Visualization, Investigation, Validation. **Weiwèn Zhao:** Conceptualization, Methodology, Investigation, Writing – review & editing, Supervision. **Decheng Wan:** Writing – review & editing, Resources, Supervision.

Declaration of competing interest

The authors declare that they have no known competing financial interests or personal relationships that could have appeared to influence the work reported in this paper.

Data availability

Data will be made available on request.

Acknowledgements

This work was supported by National Natural Science Foundation of China (Grant Nos. 51909160, 52131102, 51879159), National Key Research and Development Program of China (2022YFC2806705, 2019YFB1704200), to which the authors are most grateful.

References

- Afrana, R., 2011. *Coupled Dynamic Analysis of Cylindrical FPSO, Moorings and Riser Based on Numerical Simulation* (Master's Thesis. University of Stavanger, Norway).
- Amin, I., Dai, S., Day, S., Oterkus, S., Oterkus, E., 2022. Experimental investigation on the influence of interceptor plate on the motion performance of a cylindrical FPSO. *Ocean Eng.* 243, 110339.
- Avalos, G.O.G., Wanderley, J.B., 2018. Numerical study of forced roll oscillation of FPSO with bilge keel. *Ocean Eng.* 147, 304–317.
- Borsboom, M., Jacobsen, N.G., 2021. A generating-absorbing boundary condition for dispersive waves. *Int. J. Numer. Methods Fluid.* 93 (8), 2443–2467.
- Buchner, B., Voogt, A., 2009. Wave slamming on external turrets of FPSOs. In: *International conference on. Offshore Mechanics and Arctic Engineering* 43413, 571–577.
- Chen, S., Zhao, W., Wan, D., 2022. On the scattering of focused wave by a finite surface-piercing circular cylinder: a numerical investigation. *Phys. Fluids* 34 (3), 035132.
- Deng, S., Cai, Y., Yang, X., Song, Z., Yang, G., 2022a. Experimental study on the effects of wave and current interaction on vertical motions of a cylindrical FPSO. In: *The 32nd International Ocean And Polar Engineering Conference (OnePetro)*.
- Deng, S., Zhong, W., Yang, X., Wu, M., Fu, S., 2022b. Experimental and numerical study of the hydrodynamic features of a cylindrical FPSO considering current-induced motion. *Ocean Eng.* 262, 112263.
- Devolder, B., Rauwoens, P., Troch, P., 2017. Application of a buoyancy-modified k - ω SST turbulence model to simulate wave run-up around a monopile subjected to regular waves using OpenFOAM. *Coast Eng.* 125, 81–94.
- Dimakopoulos, A.S., Cuomo, G., Chandler, I., 2016. Optimized generation and absorption for three-dimensional numerical wave and current facilities. *J. Waterw. Port, Coast. Ocean Eng.* 142 (4), 06016001.
- Gonçalves, R.T., Fajarra, A.L., Rosetti, G.F., Nishimoto, K., Cueva, M., Siqueira, E.F., 2009. Vortex-induced motion of a monocolumn platform: new analysis and comparative study. In: *International Conference on Offshore Mechanics and Arctic Engineering*, vol. 43413, pp. 343–360.

- Gu, J.Y., Xie, Y.L., Zhang, P., Chen, Y., Huang, X.H., Tao, Y.W., 2017. Experimental study on hydrodynamic performance of a new type of deep draft multi-column FPSO. *J. Mar. Sci. Technol.* 25 (3), 9.
- Guiñón, J.L., Ortega, E., García-Antón, J., Pérez-Herranz, V., 2007. Moving average and Savitzki-Golay smoothing filters using Mathcad. *Pap. ICEE* 1–4, 2007.
- Ha, Y.J., Nam, B.W., Kim, K.H., Hong, S.Y., 2019. CFD simulations of wave impact loads on a truncated circular cylinder by breaking waves. *Int. J. Offshore Polar Eng.* 29, 306–314, 03.
- Hasselmann, D.E., Dunckel, M., Ewing, J.A., 1980. Directional wave spectra observed during JONSWAP 1973. *J. Phys. Oceanogr.* 10 (8), 1264–1280.
- Higuera, P., Lara, J.L., Losada, I.J., 2013. Realistic wave generation and active wave absorption for Navier–Stokes models: application to OpenFOAM. *Coast Eng.* 71, 102–118.
- Hong, S.K., Yuck, R.H., Jang, B.S., Kang, H.S., Kim, S.E., Seo, J.S., 2011. The investigation of non-linear effect for a circular cylinder shaped FPSO. In: *International Conference on Offshore Mechanics and Arctic Engineering*, vol. 44359, pp. 837–845.
- Hunt, J.C., Wray, A.A., Moin, P., 1988. Eddies, streams, and convergence zones in turbulent flows. Studying turbulence using numerical simulation databases. In: *Proceedings of the 1988 Summer Program*, vol. 2.
- Ji, X., Li, Y., Tang, Y., Tong, B., 2019. Viscous damping effect and vortex shedding performance of the novel anti-motion structures on a cylindrical FPSO. *Ocean. Eng.* 190, 106430.
- Jiang, M., Li, D., Wang, Z., Jia, X., Yu, Y., 2020. Hydrodynamic study on the damping characteristics of cylindrical FPSO with the heave plate. In: *International Conference on Offshore Mechanics and Arctic Engineering*, vol. 84317. American Society of Mechanical Engineers. V001T01A038.
- Liu, Y., Wan, D., 2013. Numerical simulation of motion response of an offshore observation platform in waves. *J. Mar. Sci. Appl.* 12 (1), 89–97.
- Menter, F.R., 1992. *Improved Two-Equation K-Omega Turbulence Models for Aerodynamic flows*(No. A-92183).
- Rusche, H., 2002. *Computational Fluid Dynamics of Dispersed Two-phase Flows at High Phase Fractions*. Imperial College London (University of London).
- Seok, W., Park, S.Y., Rhee, S.H., 2020. An experimental study on the stern bottom pressure distribution of a high-speed planing vessel with and without interceptors. *Int. J. Nav. Archit. Ocean Eng.* 12, 691–698.
- Sommerfeld, A., 1949. *Partial Differential Equations in Physics*. Academic press.
- Van Maele, K., Merci, B., 2006. Application of two buoyancy-modified k-ε turbulence models to different types of buoyant plumes. *Fire Saf. J.* 41 (2), 122–138.
- Wang, J., Wan, D., 2018. CFD investigations of ship maneuvering in waves using naoe-FOAM-SJTU Solver. *J. Mar. Sci. Appl.* 17 (3), 443–458.
- Wang, J.H., Zhao, W.W., Wan, D.C., 2019. Development of naoe-FOAM-SJTU solver based on OpenFOAM for marine hydrodynamics. *J. Hydrodyn.* 31 (1), 1–20.
- Yeon, S.M., Yang, J., Stern, F., 2016. Large-eddy simulation of the flow past a circular cylinder at sub-to super-critical Reynolds numbers. *Appl. Ocean Res.* 59, 663–675.
- Zhao, W.W., Wang, J.H., Wan, D.C., 2020. Vortex identification methods in marine hydrodynamics. *J. Hydrodyn.* 32 (2), 286–295.
- Zhuang, Y., Wan, D.C., 2021. Parametric study of a new HOS-CFD coupling method. *J. Hydrodyn.* 33 (1), 43–54.